MOF-derived Co/Cu-embedded N-doped Carbon for Trifunctional ORR/OER/HER Catalysis in Alkaline Media

ARTICLE

MOF-derived Co/Cu-embedded N-doped Carbon for Trifunctional ORR/OER/HER Catalysis in Alkaline Media

Angela Macedo Andrade,[a] Ziqi Liu,[b] Simranjit Grewal,[a] Art J. Nelson,[c] Ziad Nasef,[b] Gerardo Diaz,[b] and Min Hwan Lee[a,b*]

In this report, we demonstrate a bimetallic Co/Cu-embedded N-doped carbon structure for trifunctional catalysis of oxygen reduction, oxygen evolution and hydrogen evolution reactions in alkaline media. A hybrid catalyst synthesized through a metal-organic framework-based process (M-NC-CoCu) enables an active trifunctional catalysis due to its multi-faceted favorable characteristics. It is believed that a range of catalytically active sites are formed through the approach including well-dispersed tiny $CuCo_2O_4$ phases, a high concentration of pyridinic and graphitic N, and $Cu-O_x$, $Cu-N_x$ and $Co-N_x$ moieties. In addition, a high-surface-area morphology with a high concentration of sp^2 bonding, which is beneficial for facilitated electron conduction, further contributes to the performance as an electrocatalyst.

Introduction

The advancement of electrochemical energy conversion technologies such as fuel cells, water splitting systems and metal-air batteries is heavily reliant upon a range of functionalities for three essential electrochemical reactions – hydrogen evolution reactions (HER), oxygen evolution reaction (OER) and oxygen reduction reaction (ORR).[1–3] Noble metal-based catalysts have been widely used for HER (Pt), ORR (Pt) and OER (Ir and Ru) owing to their excellent electrocatalytic activity, but their high cost, scarcity, and low stability drives active development of alternative catalysts.[2,4]

Transition metals (TM) and their oxides (TMO), among many, have been widely studied as a typical class of non-noble metal-based hydrogen and oxygen electrocatalysts due to the cost-effectiveness, multi-valence and tunability of chemical composition, structure and morphology.[5,6] Cobalt (Co) is one of the most commonly used TMs for bifunctional oxygen electrocatalysis [7–12] partially because of their tendency to better absorb reactants for each reaction (i.e. O_2 for ORR and OH^- for OER).[5] To augment electrical conductivity and catalytic activity, as is the case for many other TM/TMO-based catalysts, Co and CoO_x nanoparticles are often dispersedly embedded into carbon-based structures for bifunctional electrocatalysis.[7,13,14] On the other hand, copper (Cu) is theoretically predicted to exhibit one of the best ORR activities among TMs,[15] and copper

oxides (Cu_xO) have shown good HER activity due to its low energy barrier for hydrogen adsorption.[16,17] Even though metal nanoparticles exhibit good electrocatalytic activity, due to having a larger active surface area, they often have high surface energy and fast nucleation that makes them prone to agglomeration.[18–20] To address the issue of Cu being readily agglomerated, researchers have used N-doped carbon as the template to stably anchor tiny Cu species.[21–23] The approach also rendered excellent ORR performance, which is mainly ascribed to rich $Cu-N_x$ bonds within the hybrid matrix.[6]

To overcome relatively low activity of single-TM catalysts, bimetal-based systems have attracted significant recent attention.[24–27] A multi-metallic species often induces a synergistically enhanced catalytic activity due to a favorable rearrangement of electronic structures to reduce kinetic energy barriers.[25] In addition, the introduction of a secondary metal can deter the overall agglomeration kinetics of each metal during the pyrolysis of metal-organic frameworks (MOFs),[28] a widely used approach in synthesizing TM-supporting N-doped carbon.[29,30] All the aforementioned studies considered, it is a reasonable approach to design bimetallic Co and Cu-embedded N-doped carbon systems for trifunctional electrocatalysis. There have been several recent studies on the use of Co/Cu-based bimetallic hybrids for monofunctional or bifunctional catalysis of HER, ORR and/or OER, but there has not been a report on the trifunctional capability.[16,23,26,28,29,31–35]

Herein, we demonstrate a new facile MOF-based process to realize an efficient trifunctional catalyst where tiny Cu species are uniformly dispersed in Co/CoO_x-embedded N-doped carbon. The aminoterephthalic acid organic linker used in this study not only has the carboxylic acid sites where the metals could complex but also has an amine group that can complex with metal centers and provides a nitrogen source for doping carbon.[36–38] It is believed that Co-anchored N-doped carbon

[a.] Graduate Program in Materials and Biomaterials Science and Engineering, University of California, Merced, CA 95343, USA
[b.] Department of Mechanical Engineering, University of California, Merced, CA 95343, USA
[c.] Physical and Life Science Directorate, Lawrence Livermore National Laboratory, CA 94550, USA

acts not only as an efficient OER catalyst but also as an inhibitor of Cu agglomeration for both ORR and HER. The hybrid system also has $CuCo_2O_4$ clusters (for ORR and OER) in addition to Cu-N_x, Cu-O_x (for HER and ORR), and Co-N_x complexes (for OER) in a N-doped carbon structure for further enhanced catalytic activity. The resulting heterogeneous material renders a hierarchical structure for both efficient mass transport and large surface area that demonstrates active trifunctional catalysis for ORR, OER and HER in alkaline solution.

Experimental Section

Metal-organic hybrid synthesis

0.75 mmol of $CoCl_2 \cdot 6H_2O$ (98%, Alfa Aesar) and 0.75 mmol $CuCl_2 \cdot 2H_2O$ (99+% ACS grade, Alfa Aesar) were dissolved in 20 ml of dimethylformamide (DMF, 99.8+% ACS grade, Alfa Aesar) and sonicated for 20 min. Then 1.5 mmol of 2-aminoterephthalic acid (NBDC, 99%, ACS grade, Alfa Aesar) was added to the solution and sonicated for an additional 20 min. The solution was transferred to a 40 ml autoclave for the solvothermal reaction at 140 °C for 24 h under airtight conditions. The solid was collected and rinsed several times via centrifugation using DMF, water and ethanol. After being air-dried, the sample was dried further at 150 °C under N_2 conditions for several hours to obtain NH_2-CoCu-MOF. By heat-treating the resulting solid at 800 °C for 2 h in N_2, a N-doped carbon with Co and Cu (we name it M-NC-CoCu; M-NC meaning MOF-derived N-doped carbon) was obtained. Two other variants of study, M-NC-Co and M-NC-Cu were prepared via the same approach by starting with $CoCl_2 \cdot 6H_2O$ or $CuCl_2 \cdot 6H_2O$, respectively, instead of both. It is noted that two more batches of samples heat-treated at 700 °C and 600 °C were also characterized, but those pyrolyzed at 800 °C are mainly discussed in this report due to their higher catalytic performance (see Fig. S1).
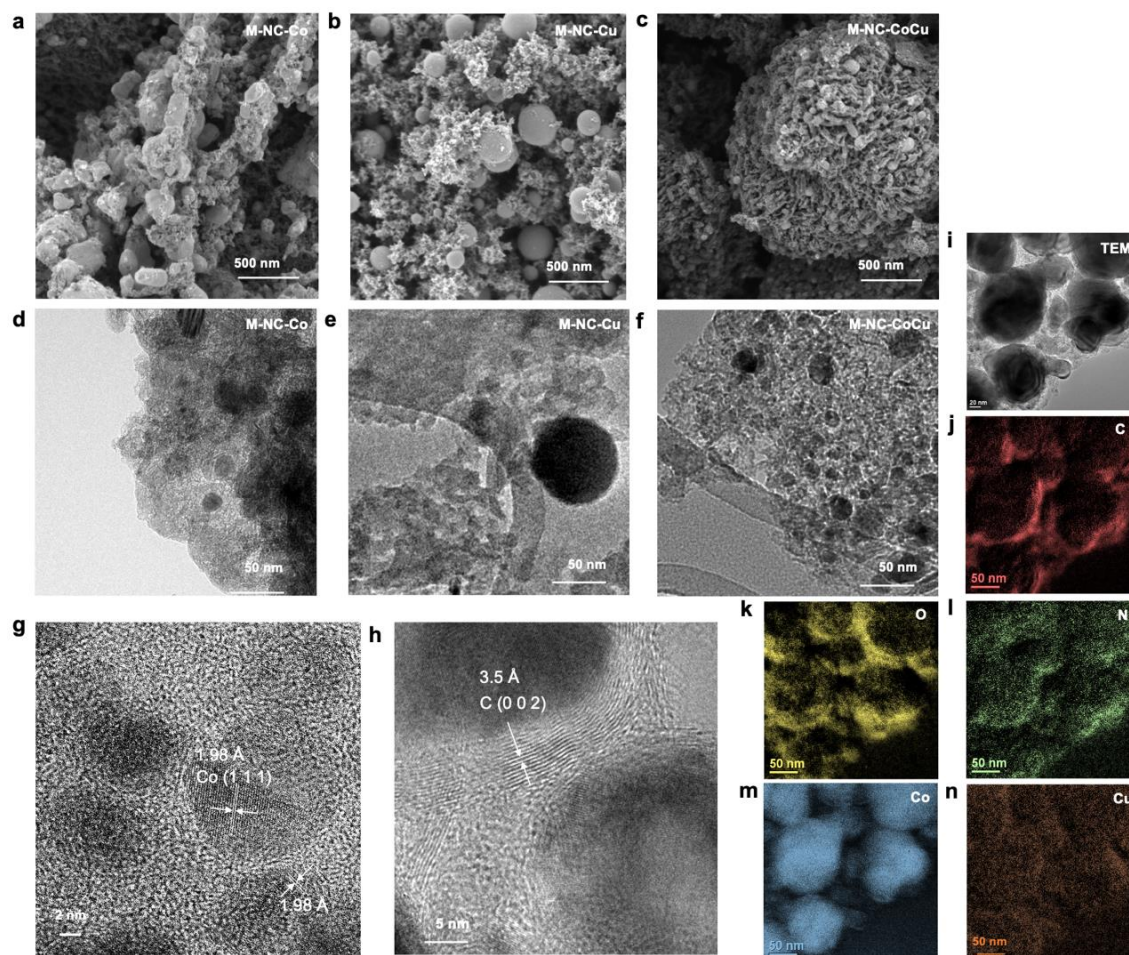
Fig. 1 SEM (a-c) and TEM (d-f) micrographs of M-NC-Co, M-NC-Cu and M-NC-CoCu. (g,h) HRTEM images of M-NC-CoCu showing lattice fringes of Co (1 1 1) and C (0 0 2). (i-n) A TEM image of M-NC-CoCu and its corresponding EFTEM elemental maps.

Material Characterization

Transmission electron microscopy (TEM) and scanning transmission electron microscopy (STEM) images were recorded on a 200 kV FEI monochromated F20 UT Tecnai system. The STEM image was acquired with a convergence angle of 10 mrad and a detection angle of 30 mrad. Energy filtered transmission electron microscopy (EFTEM) was used to visualize elemental distribution. Sample preparation for TEM samples included drop-casting ethanol-suspended catalyst upon a 3 mm Lacey B Carbon 400 mesh grid from Ted Pella, followed by ambient drying. X-ray photoelectron spectroscopy (XPS) was performed on a PHI Quantum 2000 system using a focused, monochromatic Al Kα X-ray (1486.6 eV) source for excitation and a spherical section analyzer (200 μm diameter X-ray beam incident to the surface normal; detector set at 45°). The collected data were referenced to an energy scale with binding energies for Cu $2p_{3/2}$ at 932.7 ± 0.1 eV and Au $4f_{7/2}$ at 84.0 ± 0.1 eV. For XPS, catalysts were dispersed in ethanol and drop-cast onto a cleaned Si wafer. X-ray diffraction (XRD) pattern was recorded by a PANalytical X'Pert PRO with Co Kα radiation (λ = 1.7890 Å) at a step size of 0.02° and scanning rate of 0.04° s^{-1}. The obtained data were converted to Cu Kα radiation (λ = 1.5406 Å)-based spectra for facile comparison with other reports. The dried powder sample was placed on the surface and flattened on the surface of a p-type boron doped silicon zero diffraction plate. FT-IR samples were dried under vacuum for 24 h by placing samples in a desiccator overnight and placed on a diamond crystal (Nicolet 380 system, Thermo Scientific). Raman spectra were obtained on an iXR Raman spectrometer (Thermo Scientific). Brauner Emmet Teller (BET) nitrogen adsorption tests were performed on a Gemini VII 2390a. The measurement test tubes were cleaned by ultrasonication with DI water and kept in the oven at 110° C for 2 h before introducing samples. Degassing was done by FlowPrep 060 for 2 h with N_2 at 250° C.

Electrochemical Characterization

Test sample preparations: The working electrode was prepared by drop-casting each electrode ink onto a glassy carbon (GC) disk electrode or nickel (Ni) foam. The Ni foam was immersed and ultrasonicated sequentially in acetone, 6 M HCl, DI water and ethanol for 30 min each and then dried at room temperature to clean and activate its surface before being deposited with catalysts of study. The ink was prepared by immersing 5 mg of hybrid catalyst materials into 1 ml of 2:1 volume of ethanol to MiliQ water along with 10.75 μl of 5 wt% Nafion (Nafion D-521, Alfa Aesar). For Pt/C electrode, a 5 mg ml^{-1} Pt/C suspension was prepared by using a commercial 20 wt% Pt supported on carbon black (Vulcan XC72). These samples were dried under N_2 at 2 standard cubic feet per hour (scfh). The loading mass for all samples measured on glassy carbon was 0.4 mg/cm^2.

Post-cycle sample preparations: Another set of samples for post-cycle XRD, XPS and SEM analysis are prepared using as-prepared M-NC-CoCu deposited on a carbon paper. M-NC-CoCu-KOH was prepared by submerging M-NC-CoCu in 1 M KOH for 12 h. Three types of post-cycle samples are prepared by cycling M-NC-CoCu for 2,000 cycles in ORR (0.2 V – 1.2 V in 0.1 M KOH), OER (1.0 V – 2.0 V in 1 M KOH) and HER conditions (-0.3 V - 0.3 V in 1 M KOH), each named as M-NC-CoCu-ORR, M-NC-CoCu-OER and M-NC-CoCu-HER, respectively.

Electrochemical characterization: The catalytic activity was evaluated with linear sweep voltammetry (LSV) using a potentiostat (SP-200, Bio-Logic Science Instruments) in either ring-disk electrode (RDE) or rotating ring-disk electrode (RRDE) setup (RRDE-3A, ALS Co. Ltd). Measurements were performed in a three-electrode setup with a graphite rod as the counter and Ag/AgCl (3.5 M KCl) or Hg/HgO (1 M NaOH) electrode as the reference electrodes. O_2 and N_2 saturated environments were implemented by flowing high-purity O_2 and N_2 gas at 2 scfh into 80 ml of electrolyte for 30 min. All electrochemical data were expressed with respect to the reversible hydrogen electrode (RHE).

Results and Discussion

Three metal/N-doped hybrid catalysts (M-NC-Co, M-NC-Cu and M-NC-CoCu) are mainly studied. Briefly, these catalysts are obtained by pyrolyzing Co and/or Cu-based MOF structures, which were synthesized by using $CoCl_2$ and/or $CuCl_2$ as the metal precursors and NBDC as the organic ligand (see Experimental for details). In all three samples, the spherical species, which corresponds to metal species (Co, Cu or their oxides) as will be revealed by TEM and XRD below, are well dispersed within a porous carbon matrix as shown in the SEM (Figs. 1a-c) and TEM images (Figs. 1d-f). The sizes of metal clusters in M-NC-Co and M-NC-Cu span up to hundreds of nanometers whereas those of M-NC-CoCu are significantly smaller with a more uniform distribution in size. This is in accordance with recent studies reporting the suppression of metal particle agglomerations by the introduction of a secondary metal in a MOF-based synthesis.[28,39] The SEM micrographs show that the carbon matrix of M-NC-CoCu is in a pinecone-like shape while the geometry of the other two samples are less defined. The precursor structure for M-NC-CoCu (i.e., the MOF structure for M-NC-CoCu prior to the pyrolysis; namely, NH_2-NC-CoCu-MOF) also exhibits a pinecone-like feature but with a somewhat larger size (Fig. S3). None of the major XRD peaks (Fig. S4) from the MOF (NH_2-NC-CoCu-MOF) corresponds to those of metal precursors ($CoCl_2$, $CuCl_2$) or NBDC linker, indicating a complete rearrangement of atomic structure during the MOF synthesis process. This is further supported by the absence of Cl 1s peak in the XPS spectrum of NH_2-NC-CoCu-MOF (Fig. S5) and the absence of Cl peak from the EDS spectrum of M-NC-CoCu (Fig. S6). The HRTEM images of M-NC-CoCu show nanoparticles of metallic Co (Fig. 1g; *d*-spacing = 1.98 Å corresponding to Co (1 1 1) planes) encapsulated by graphitic carbon layers (Fig. 1h; *d*-spacing of ~ 3.5 Å corresponding to C (0 0 2) plane).[40] The elemental maps of Co
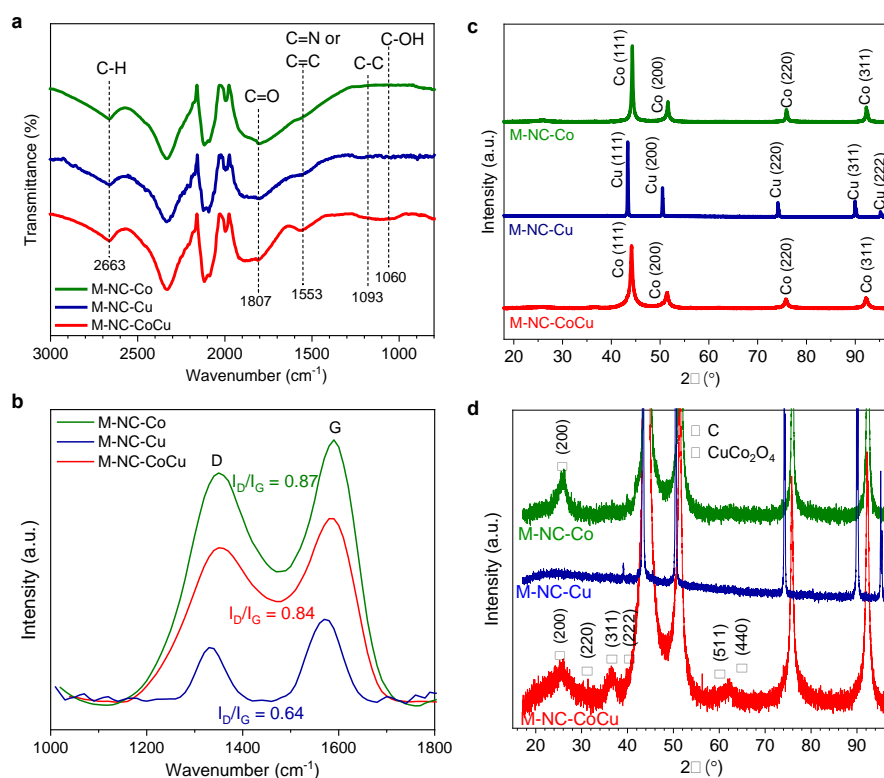
Fig. 2 (a) FT-IR spectra, (b) Raman spectra and (c,d) XRD spectra of the three samples. (d) shows zoomed-in spectra of (c) for clarity.

and Cu in M-NC-CoCu (Figs. 1m and 1n) reveal that Co species form nanoclusters while seemingly much smaller Cu are uniformly dispersed. Meanwhile, the O species (Fig. 1k) tend to reside where C species are located but a significantly lower O concentration is observed on Co nanoclusters, hinting most Co species are mostly in the metallic state. The N mapping (Fig. 1l) also suggests uniform and dense N-doping in the carbon matrix. Fourier transform infrared spectroscopy (FT-IR) spectra (Fig. 2a) shows that M-NC-CoCu has a distinct presence of sp^2 C=N and C=C bonds,[41] unlike the other two hybrid catalysts. The larger amount of sp^2 bonds in M-NC-CoCu should provide a higher electronic conductivity through the carbon structure,[42,43] making it advantageous for electrode performance. The peaks located at $2000 - 2300$ cm^{-1} are ascribed to ambient CO_2. Meanwhile, Raman spectra of all the three samples show distinct G (ca. 1590 cm^{-1}) and D peaks (ca. 1340 cm^{-1}) as presented in Fig. 2b. It is widely known that both peaks are originated from vibrations of sp^2 carbon, but the appearance of D peak is ascribed to the presence of defects caused by disordered structures and heteroatom doping while the G peak corresponds to the in-plane bond stretching of sp^2 carbon pairs.[44,45] Higher I_D/I_G ratios of M-NC-CoCu (0.84) and M-NC-Co (0.87), compared to that of M-NC-Cu (0.64), are in part ascribed to their higher N doping in the carbon (as shown below from XPS). The XRD spectra (Fig. 2c) shows a dominant presence of cubic Co in M-NC-Co and cubic Cu in M-NC-Cu. The average sizes of Co in M-NC-Co and Cu in M-NC-Cu quantified by applying the

Scherrer equation[46] to their (1 1 1) peaks are 44.3 and 73.8 nm, respectively. Interestingly, the spectrum for M-NC-CoCu has peaks mostly corresponding to cubic Co without a trace of monometallic Cu. The average size of Co in M-NC-CoCu (27.7 nm) is much smaller than that of M-NC-Co, which is in accordance with the SEM images in Fig. 1. Most of the other tiny peaks found in M-NC-CoCu (Fig. 2d) are attributed to spinel $CuCo_2O_4$ (Fm-3m:2 space group).[23,31,47] The average size of $CuCo_2O_4$ crystals quantified by applying the Scherrer equation to the (3 1 1) peak is 4.3 nm, which is significantly smaller than Co (33.7 nm) found in the same sample. It is also noted that the small graphitic peak at $2\theta = 25.6°$ corresponding to (0 0 2) carbon plane is visible in M-NC-Co and M-NC-CoCu (Fig. 2d), which is also aligned with the aforementioned HRTEM observation (Fig. 1h). The average thicknesses of the graphitic layers estimated again by the Scherrer equation are 3.52 nm for M-NC-Co and 1.80 nm for M-NC-CoCu. An encapsulation of Cu by graphitic carbon is known to be difficult to achieve via an *in situ* carbonization of MOFs due to the fast nucleation of Cu,[48] explaining the absence of the graphitic diffraction peak (Fig. 2d) and the large Cu particle sizes in M-NC-Cu (Fig. 1b).

X-ray photoelectron spectra (XPS) analysis was conducted for a better understanding of the chemical bonding in these samples. In the survey spectra for the three hybrid samples, Co, Cu, O, N, and C were detected (Fig. S7). The N 1s spectra shows peaks for graphitic (402.2 eV), pyrrolic (400.7 eV) and pyridinic (398.7 eV) nitrogen for all three samples (Fig. 3a),[23,49,50] confirming a
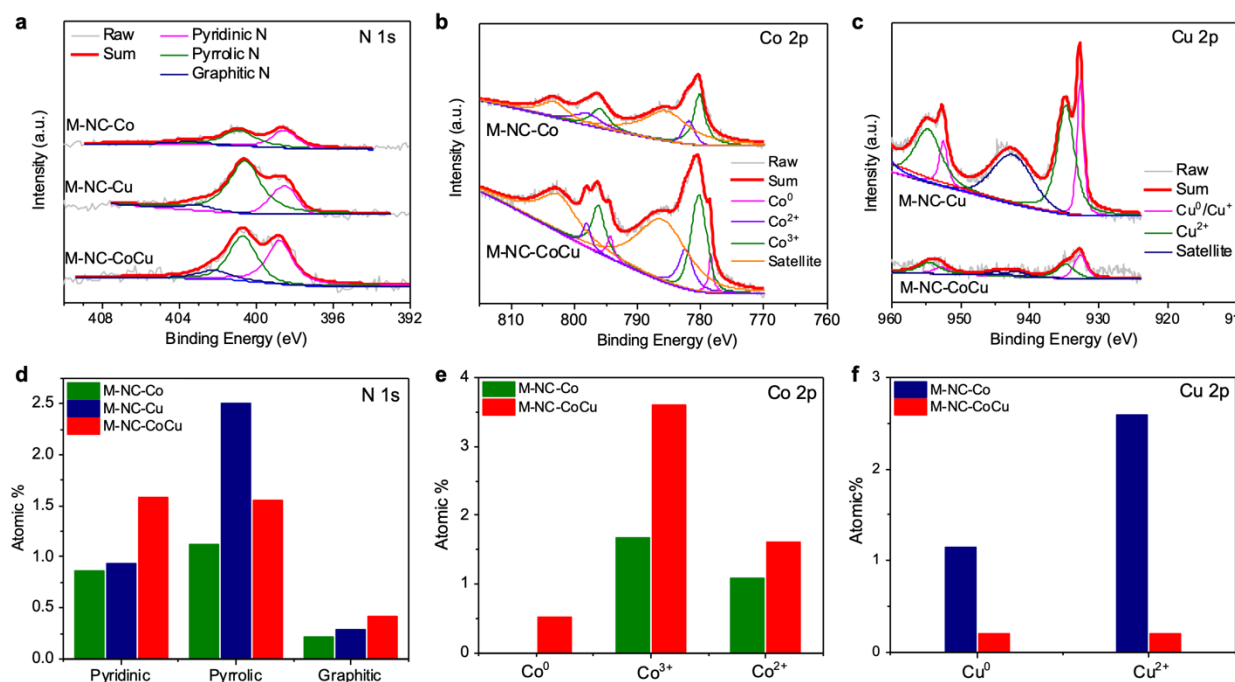
Fig. 3 (a-c) XPS spectra of N 1s (a), Co 2p (b) and Cu 2p (c); (d-f) the atomic percentages of species quantified based upon spectra fitting.

considerable amount of N-doping in the supporting carbon structures. The M-NC-Cu and M-NC-CoCu samples are quantified to have higher N contents (Fig. 3d; 3.7 and 3.6 at%) than M-NC-Co (2.8 at%). This is ascribed to the presence of Cu, which readily complexes with N and retains N even after thermal treatments,[23] forming more catalytically active Cu-N$_x$ moieties.[48,51] It is also noted that M-NC-CoCu has the highest amount of pyridinic and graphitic N (Fig. 3d), both of which are known to contribute to ORR and HER activity.[23,33,52–56] We also note that the M-NC-CoCu has a distinct metallic Co peak (778.4 eV) unlike M-NC-Co (Fig. 3b). While M-NC-Co showed a strong presence of metallic Co phase in XRD (Fig. 2c), no metallic Co peak is detected by XPS, indicating Co was oxidized on its surface. In contrast, the metallic Co peak detected from M-NC-CoCu is possibly because the graphitic layer that encased the Co nanoparticles (as seen in Fig. 1h) protects the Co from oxidation.[8,23,57] Two oxidized Co species, Co^{3+} (780.2 eV) and Co^{2+} (781.9 eV) are present with a Co^{3+}/Co^{2+} ratio of 1.52 and 2.22 for M-NC-Co and M-NC-CoCu, respectively (Fig. 3e). The higher Co^{3+}/Co^{2+} ratio of M-NC-CoCu supports the presence of spinel CuCo$_2$O$_4$ in the sample; in the spinel structure, Cu occupies tetrahedral sites making Co species sit in octahedral sites with high valence state.[31] Furthermore, spinel CuCo$_2$O$_4$ is considered to be highly active toward ORR and OER,[31,35,58,59] which is well aligned with the excellent catalytic performance of M-NC-CoCu (discussed below). In the N 1s spectra, the pyridinic N peak (398.6 eV) can also be ascribed to the catalytically active Co-N and/or Cu-N bonds given their similar binding energies.[50,60] The Cu 2p spectra of M-NC-Cu and M-NC-CoCu

have two main peaks, one associated with metallic Cu or Cu$^+$ species (932.7 eV) and the other corresponding to Cu^{2+} (934.8 eV). Both Cu$^+$ and Cu^{2+} are assigned to unsaturated Cu–N centers,[23,45,48,61] while Cu^{2+} is additionally assigned to Cu–O in the spinel structure and Cu-O$_x$.[31] The aforementioned Cu elemental map (Fig. 1m) showed that Cu species are uniformly dispersed on both Co nanoclusters and carbon matrix. Those dispersed on Co clusters is ascribed to small crystalline domains of CuCo$_2$O$_4$, and those located on the carbon matrix are presumed to form Cu-N-C and Cu-O-C, as opposed to crystalline clusters of monometallic cubic Cu. The N 1s spectra also suggests the presence of Cu-N$_x$, which has been assigned for ~398.5 eV.[22,45,60]

The oxygen electrocatalytic performance of the three hybrid samples is compared with noble metal-based benchmark catalysts: Pt/C for ORR and HER, and IrO$_2$ for OER. The ORR voltammograms in 0.1 M KOH (Fig. 4a) shows that M-NC-CoCu performs the best among the three hybrids with onset potential (E_{on}) and half-wave potential ($E_{1/2}$) of 0.85 V and 0.75 V (versus RHE hereafter), comparable to those of Pt/C (E_{on} = 0.93 V; $E_{1/2}$ = 0.82 V). M-NC-CoCu also affords a small Tafel slope (63 mV dec^{-1}; Fig. 4d), even lower than Pt/C (70 mV dec^{-1}) indicating its fast ORR kinetics. In addition, M-NC-CoCu exhibits a dominant four-electron process with the electron transfer number (n) of 3.9 − 4.0 in the wide potential window of 0.2 − 0.8 V (Fig. S8), unlike the other two hybrids rendering a mixed 2e$^-$ and 4e$^-$ transfer (n = 2.48 and 3.28 for M-NC-Cu and M-NC-Co at 0.4 V). As for OER, M-NC-CoCu still exhibits the best performance among the hybrid catalysts, reaching 10 mA cm^{-2} in 1 M KOH at the lowest
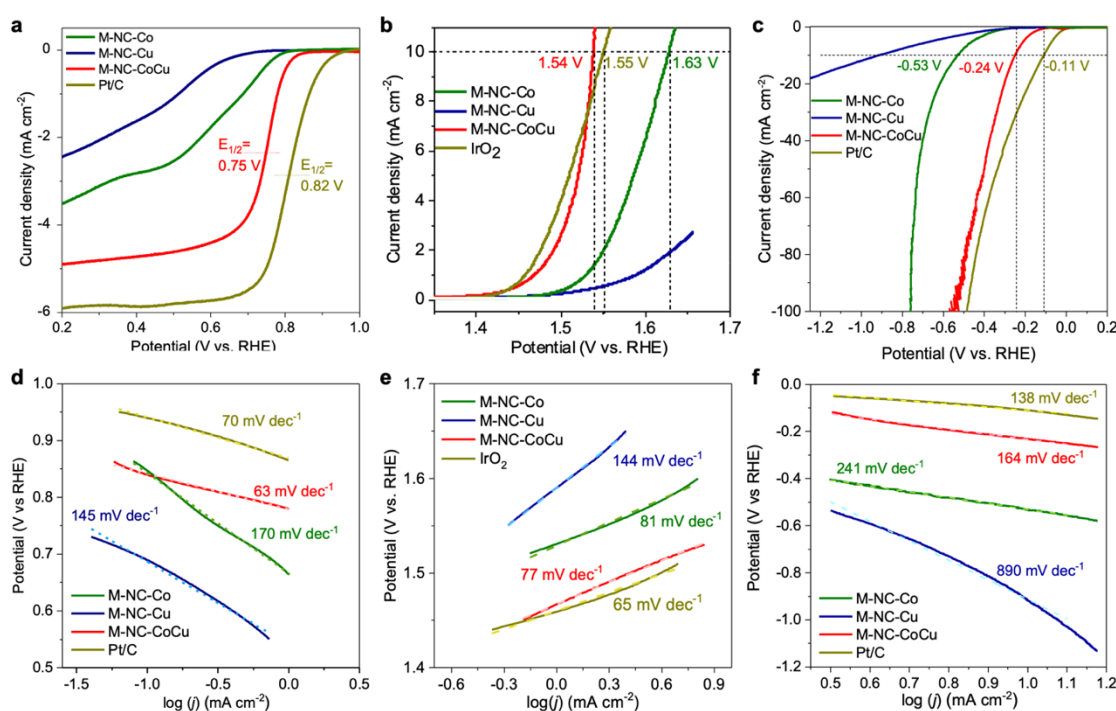
Fig. 4 (a-c) LSV voltammograms for ORR (a), OER (b) and HER (c). (d-f) Tafel plots along with Tafel slope values for ORR (d), OER (e) and HER (f). All quantified at 1600 rpm. ORR voltammograms are obtained in 0.1 M KOH while OER and HER voltammograms are obtained in 1 M KOH.

potential of 1.54 V ($E_{j=10}$ = 1.54 V; Fig. 4b), slightly smaller than the value for IrO_2 (1.55 V). Its Tafel slope is also the smallest (77 mV dec^{-1}; Fig. 4e) among the three hybrids, close to that of IrO_2 (65 mV dec^{-1}). It is noted that the OER LSV shown in Fig. 5b is obtained from catalysts deposited on a Ni foam (unlike the LSVs for ORR and HER that are measured in an RDE setup), and that $E_{j=10}$ of bare Ni foam (1.63 V) is significantly larger than that of M-NC-CoCu as shown in Fig. S9. Even for HER, M-NC-CoCu shows the lowest overpotential among the hybrid samples with $E_{j=10}$ = -0.24 V to reach 10 mA cm^{-2} (Fig. 4c), the closest to that of Pt/C ($E_{j=10}$ = -0.11 V). Both M-NC-CoCu and Pt/C have the smallest Tafel slope (Fig. 4f) with 164 mV dec^{-1} and 138 mV dec^{-1}, respectively. Additionally, turnover frequencies (TOFs) and mass activities of all three hybrid catalysts and benchmark catalyst are quantified for ORR, OER and HER (Fig. S10). Especially for OER, M-NC-CoCu shows a higher TOF (1.26 s^{-1}) and mass activity (47.6 A g^{-1}) than IrO_2 (0.14 s^{-1} and 24.9 A g^{-1}, respectively; all quantified at the overpotential of 330 mV), confirming its excellent intrinsic OER activity. For HER and ORR, TOFs and mass activities of M-NC-CoCu are somewhat lower than those of Pt/C.

The reasons for the trifunctional capability of M-NC-CoCu can be summarized as follows. First, M-NC-CoCu has $CuCo_2O_4$ phases, which has been reported to be active toward ORR and OER.[35,58,59] Additionally, the highly dispersed Cu-N$_x$ and Cu-O$_x$ moieties and the largest amount of graphitic and pyridinic N-doping should further contribute to the ORR, OER and HER

activities. The unsaturated nature of Cu-N$_x$ centers (with Cu$^+$ and Cu^{2+}) become active sites for ORR due to the unfilled 3d-orbital electrons that can contribute to the electronic interactions with oxygen intermediates, which results in ideal chemisorption of oxygen.[48] It has been reported that a direct high-temperature pyrolysis of Co-based MOFs tends to result in a severe agglomeration of Co atoms, reducing the amount of atomic Co-N$_x$ dispersion.[62] As the size of Co particles in M-NC-CoCu is significantly smaller than those of M-NC-Co due to the presence of a second metal (Cu), M-NC-CoCu is likely to have more of atomic Co-N$_x$ moieties benefiting the overall catalytic activity. The high concentrations of sp^2 bonding are also expected to enhance electronic conductivity of the matrix, and the well-defined 3D structure along with uniformly-dispersed catalytically-active species should also be synergistically beneficial to the performance. A separately quantified electrochemically active surface area (ECSA; represented by double layer capacitance, C_{dl}) of M-NC-CoCu is indeed found to be the highest by a significant margin among the hybrid catalysts. The C_{dl} values of M-NC-Co, M-NC-Cu and M-NC-CoCu are 4.0, 6.2 and 14.0 mF cm^{-2}, respectively (Fig. S11). When quantified from BET N_2 isotherms (Fig. S12), however, the surface area (SA) of M-NC-CoCu (242.8 m^2 g^{-1}) is similar to that of M-NC-Co (240.5 m^2 g^{-1}) but significantly larger than that of M-NC-Cu (110.0 m^2 g^{-1}). The discrepancy between BET SA and
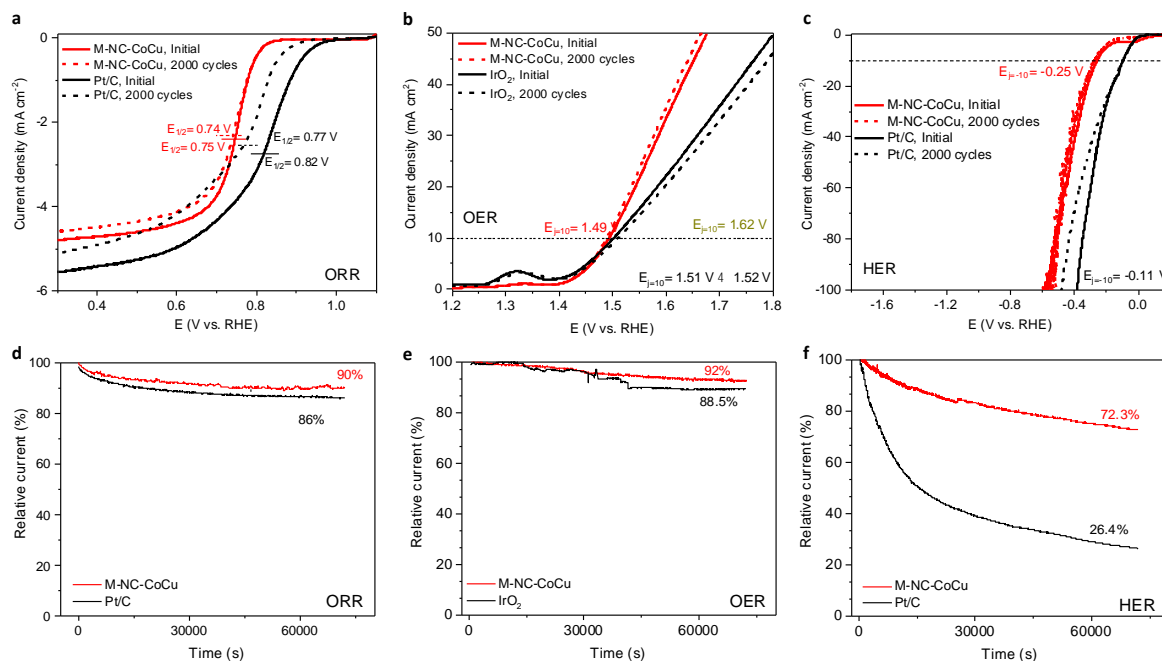
Fig. 5 (a-c) Cyclic stability of M-N-CoCu and noble metal benchmarks for ORR (a), OER (b) and HER (c). The potential range of cycling is 0.2 − 1.2 V for ORR, 1 − 2 V for OER and -0.1 − 0.3 V for HER. Quantified at 1600 rpm in 0.1 M KOH for ORR, in 1 M KOH for HER, and in a stationary condition on a Ni foam in 1 M KOH for OER. (d-f) chronoamperometric stability evaluation of M-NC-CoCu and benchmarks for ORR in 0.1 M KOH at 0.5 V (d), OER in1 M KOH at 1.55 V (e), and HER in 1 M KOH at -0.3 V (f). All the chronoamperometric measurements were performed on a glassy carbon.

ECSA in terms of the relative surface area among the samples should be mainly because the catalytically active SA is only a subset of the total SA.[63] The BET analysis provides a more accurate estimation of the total SA and thus is prone to overestimate the catalytically active SA while the ECSA is a better descriptor of catalytically relevant SAs.[63]

Additionally, the durability of the best performing sample (M-NC-CoCu) is characterized by cyclic measurements in the potential window of 0.2 V − 1.2 V for ORR (in 0.1 M KOH), 1.0 V − 2.0 V for OER (in 1 M KOH) and -0.3 V - 0.3 V for HER (in 1 M KOH), and compared to those of noble metal benchmarks. For ORR, M-NC-CoCu shows a slight change in $E_{1/2}$ (from 0.75 V to 0.74 V) after 2,000 cycles whereas Pt/C showed a significant degradation by decreasing $E_{1/2}$ from 0.82 V to 0.77 V (Fig. 5a). For both OER and HER, M-NC-CoCu shows impressive cycling durability; there is little change in the current-potential profile after 2,000 cycles (Figs. 5b and 5c). On the other hand, IrO_2 for OER shows a noticeable degradation by increasing $E_{j=10}$ from 1.51 V to 1.52 V. The degradation is more pronounced at higher current densities; the potential to reach j = 40 mA cm^{-2} increased from 1.73 V to 1.76 V. For HER, Pt/C also exhibits a clear degradation after 2,000 cycles unlike M-NC-CoCu. It is noted that the discrepancy between OER voltammograms shown in Figs. 4b and 5b is originated from the different setup they are obtained; the cycle durability test for OER was performed by placing the samples on a Ni foam whereas all the electrochemical measurements including ORR durability test was performed on a rotating glassy carbon. Oxygen gas

bubbling from a continuous OER prevented stable voltammetry in the rotating glassy carbon setup. A set of chronoamperometric stability test results are also presented in Figs. 5d-f. M-NC-CoCu exhibits a superior stability over benchmark catalysts (Pt/C for ORR and HER; IrO_2 for OER), consistent with the aforementioned cyclic durability tests. M-NC-CoCu maintains larger than 90% of its initial current even after a continuous operation at 0.5 V (ORR) and 1.55 V (OER) for > 70,000 s. While the hybrid catalyst shows a lower stability for HER (72.3% at -0.3 V), its stability is much better than that of Pt/C (26.4%) under the same condition.

To examine changes in chemical states and phases of M-NC-CoCu during operation, XRD and XPS are additionally performed after submerging it in 1 M KOH for 12 h (the resulting sample named M-NC-CoCu-KOH) and after a 2,000 cycling in potential regions pertaining to OER (M-NC-CoCu-OER), HER (M-NC-CoCu-HER) and ORR (M-NC-CoCu-ORR); the procedure of sample preparation is detailed in the Experimental section. Exposure to extensive electrochemical cycling results in changes in the chemical states of the constituent elements and phases although little degradation in the electrochemical performance is incurred during the same cyclic operation. First, compared to the as-prepared sample (M-NC-CoCu), M-NC-CoCu-KOH shows a decrease in intensity in both metallic Co^0 (ca. 778 eV in Fig. 6b) and Cu$^{0/1+}$ (ca. 933 eV in Fig. 6c), which is likely due to the formation of hydroxides on the surface.[64,65] However, the XRD peaks corresponding to $CuCo_2O_4$, Co_3O_4 and CoOOH become
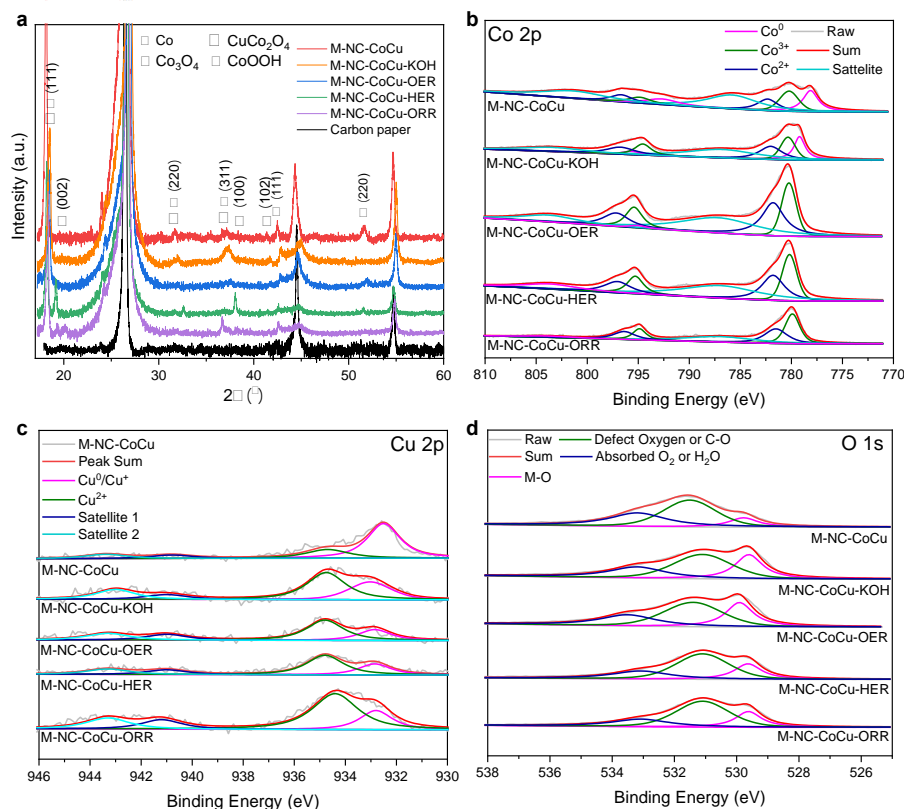
Fig. 6 (a) XRD and (b-d) XPS spectra of samples after electrochemical durability cycling. (b) Co 2p, (c) Cu 2p, (d) N1s. (e-f) Relative atomic percentage (%) of species deduced from (a) wide scan spectra of the samples and the XPS spectra shown in (b-d). It is noted that these post-cycle samples are fabricated on a carbon paper, unlike those used for physical and electrochemical characterization presented in Figs. 1-5.

intact or even stronger (Fig. 6a). After long-term cycles for ORR, OER and HER, Co^0 species in Co 2p spectra are no longer observed, and both Co and Cu are oxidized. This is corroborated by a significant decrease in the intensity of cubic Co phase from the XRD spectra and the increase of lattice oxygen content (M-O species) as shown in O 1s spectra (Fig. 6d). After OER cycles (M-NC-CoCu-OER), the Co^{3+}/Co^{2+} ratio increased from 0.91 to 1.09 (Fig. S14c), which is ascribed to the formation of CoOOH during OER resulting in the cationic oxidation.[66,67] In addition, O 1s spectra (Fig. 6d) shows an increase in the peak associated with defect oxygen (45% to 54%; Fig. S14d) and a decrease in M-O peak (27% to 22%), suggesting surface oxygen vacancy formation. After ORR cycling, there is a well-defined narrow XRD peak around corresponding to spinel Co_3O_4 and/or $CuCo_2O_4$. After HER cycles (M-NC-CoCu-HER), on the other hand, the peak at ca. 37.7° pertaining CoOOH becomes prominent.

Conclusions

In this study, we demonstrated a facile synthesis of an efficient trifunctional electrocatalyst where Co/Cu species are incorporated in high-surface-area N-doped carbon structure. The facile synthesis approach of MOF formation followed by a pyrolysis process formed highly dispersed catalytically-active sites in a hierarchical N-doped carbon. The presence of both Cu and Co species is conjectured to have deterred the agglomeration of each other and form well-dispersed active sites such as $Cu-N_x$, $Cu-O_x$ and $CuCo_2O_4$. The excellent electrocatalytic performance of M-NC-CoCu can be ascribed to multiple factors: (1) the high-surface-area structure of carbon matrix, (2) uniformly distributed tiny-sized catalytically active sites such as $CuCo_2O_4$ phases as well as $Cu-N_x$, $Cu-O_x$, and $Co-N_x$ moieties, (3) high concentration of graphitic and pyridinic nitrogen, and (4) high concentration of sp^2 bonding beneficial for electronic conduction. The multitude of active sites derived from bimetallic Cu and Co species and N-doped carbon support of M-NC-CoCu prove to be effective in catalyzing ORR, OER and HER. This study suggests that a bimetallic mixture and doping can result in multiple favorable effects that can be highly leveraged for efficient trifunctional electrocatalyst.

Conflicts of interest

There are no conflicts to declare.

Acknowledgements

ARTICLE

Notes and references

1   S. Sui, X. Wang, X. Zhou, Y. Su, S. Riffat and C. jun Liu, *J. Mater. Chem. A*, 2017, **5**, 1808–1825.

2   Z. Chen, D. Higgins, A. Yu, L. Zhang and J. Zhang, *Energy Environ. Sci.*, 2011, **4**, 3167.

3   Z. L. Wang, D. Xu, J. J. Xu and X. B. Zhang, *Chem. Soc. Rev.*, 2014, 43, 7746–7786.

4   W. T. Hong, M. Risch, K. A. Stoerzinger, A. Grimaud, J. Suntivich and Y. Shao-Horn, *Energy Environ. Sci.*, 2015, **8**, 1404–1427.

5   H. Osgood, S. V. Devaguptapu, H. Xu, J. Cho and G. Wu, *Nano Today*, 2016, **11**, 601–625.

6   C. Zhang, W. Zhang and W. Zheng, *ChemCatChem*, 2019, **11**, 655–668.

7   Y. Liang, Y. Li, H. Wang, J. Zhou, J. Wang, T. Regier and H. Dai, *Nat. Mater.*, 2011, **10**, 780–786.

8   A. Aijaz, J. Masa, C. Rösler, W. Xia, P. Weide, A. J. R. Botz, R. A. Fischer, W. Schuhmann and M. Muhler, *Angew. Chemie Int. Ed.*, 2016, **55**, 4087–4091.

9   H. Yang, Y. Zhang, F. Hu and Q. Wang, *Nano Lett.*, 2015, **15**, 7616–7620.

10   P. J. Zambiazi, G. de O. Aparecido, T. V. de B. Ferraz, W. S. J. Skinner, R. G. Yoshimura, D. E. B. Moreira, R. L. Germscheidt, L. L. Nascimento, A. O. T. Patrocinio, A. L. B. Formiga and J. A. Bonacin, *Dalt. Trans.*, 2020, **49**, 16488–16497.

11   R. K. Tripathy, A. K. Samantara and J. N. Behera, *Dalt. Trans.*, 2019, **48**, 10557–10564.

12   Z. Zhang, Y. Tan, T. Zeng, L. Yu, R. Chen, N. Cheng, S. Mu and X. Sun, *Nano Res.*, , DOI:10.1007/s12274-020-3234-6.

13   Y. Su, Y. Zhu, H. Jiang, J. Shen, X. Yang, W. Zou, J. Chen and C. Li, *Nanoscale*, 2014, **6**, 15080–15089.

14   T. Y. Ma, S. Dai, M. Jaroniec and S. Z. Qiao, *J. Am. Chem. Soc.*, 2014, **136**, 13925–13931.

15   J. K. Nørskov, J. Rossmeisl, A. Logadottir, L. Lindqvist, J. R. Kitchin, T. Bligaard and H. Jónsson, *J. Phys. Chem. B*, 2004, **108**, 17886–17892.

16   M. Kuang, P. Han, Q. Wang, J. Li and G. Zheng, *Adv. Funct. Mater.*, 2016, **26**, 8555–8561.

17   M. Jung, J. Scott, Y. H. Ng, Y. Jiang and R. Amal, *Int. J. Hydrogen Energy*, 2014, **39**, 12499–12506.

18   S. Rasul, D. H. Anjum, A. Jedidi, Y. Minenkov, L. Cavallo and K. Takanabe, *Angew. Chemie*, 2015, **127**, 2174–2178.

19   H. Tabassum, W. Guo, W. Meng, A. Mahmood, R. Zhao, Q. Wang and R. Zou, *Adv. Energy Mater.*, 2017, **7**, 1–7.

20   S. S. A. Shah, L. Peng, T. Najam, C. Cheng, G. Wu, Y. Nie, W. Ding, X. Qi, S. Chen and Z. Wei, *Electrochim. Acta*, 2017, **251**, 498–504.

21   F. Li, G. F. Han, H. J. Noh, S. J. Kim, Y. Lu, H. Y. Jeong, Z. Fu and J. B. Baek, *Energy Environ. Sci.*, 2018, **11**, 2263–2269.

22   Q. Lai, Y. Zhao, J. Zhu, Y. Liang, J. He and J. Chen, *ChemElectroChem*, 2018, **5**, 1822–1826.

23   M. Kuang, Q. Wang, P. Han and G. Zheng, *Adv. Energy Mater.*, 2017, **7**, 1700193.

24   H. Osgood, S. V Devaguptapu, H. Xu, J. Cho and G. Wu, *Nano Today*, 2016, **11**, 601–625.

25   L. Yan, L. Cao, P. Dai, X. Gu, D. Liu, L. Li, Y. Wang and X. Zhao, *Adv. Funct. Mater.*, 2017, **27**, 1703455.

26   C. Wu, M. Zhang, F. Chen, H. Kang, S. Xu and S. Xu, *Dalt. Trans.*, 2020, **49**, 13339–13344.

27   J. K. Das, A. K. Samantara, S. Satyarthy, C. S. Rout and J. N. Behera, *RSC Adv.*, 2020, **10**, 4650–4656.

28   X. Han, X. Ling, Y. Wang, T. Ma, C. Zhong, W. Hu and Y. Deng, *Angew. Chemie Int. Ed.*, 2019, **58**, 5359–5364.

29   P. Liu, Y. Hu, X. Liu, T. Wang, P. Xi, S. Xi, D. Gao and J. Wang, *J. Mater. Chem. A*, 2019, **7**, 12851–12858.

30   M. K. Sahoo, A. K. Samantara and J. N. Behera, *Inorg. Chem.*, 2020, **59**, 12252–12262.

31   H. Cheng, M.-L. Li, C.-Y. Su, N. Li and Z.-Q. Liu, *Adv. Funct. Mater.*, 2017, **27**, 1701833.

32   Z. Li, T. Yang, W. Zhao, T. Xu, L. Wei, J. Feng, X. Yang, H. Ren and M. Wu, *ACS Appl. Mater. Interfaces*, 2019, **11**, 3937–3945.

33   H. Zhang, Z. Yang, X. Wang, S. Yan, T. Zhou, C. Zhang, S. G. Telfer and S. Liu, *Nanoscale*, 2019, **11**, 17384–17395.

34   W. Niu, J. Shi, L. Ju, Z. Li, N. Orlovskaya, Y. Liu and Y. Yang, *ACS Catal.*, 2018, **8**, 12030–12040.

35   X. Wang, Y. Li, T. Jin, J. Meng, L. Jiao, M. Zhu and J. Chen, *Nano Lett.*, 2017, **17**, 7989–7994.

36   A. Rotondo, G. Bruno, G. Brancatelli, F. Nicolò and D. Armentano, *Inorganica Chim. Acta*, 2009, **362**, 247–252.

37   W.-Z. Li, Y. Zhou, F. Liu, Y. Li, M.-J. Xia, E.-H. Han, T. Wang, X. Zhang and Y. Fu, *Nanomaterials*, 2017, **7**, 237.

38   Y. Yang, R. Lin, L. Ge, L. Hou, P. Bernhardt, T. E. Rufford, S. Wang, V. Rudolph, Y. Wang and Z. Zhu, *Dalt. Trans.*, 2015, **44**, 8190–8197.

39   P. Yin, T. Yao, Y. Wu, L. Zheng, Y. Lin, W. Liu, H. Ju, J. Zhu, X. Hong, Z. Deng, G. Zhou, S. Wei and Y. Li, *Angew. Chemie*, 2016, **128**, 10958–10963.

40   B. Y. Xia, Y. Yan, N. Li, H. Bin Wu, X. W. Lou and X. Wang, *Nat. Energy*, 2016, **1**, 15006.

41   T. Van Khai, H. G. Na, D. S. Kwak, Y. J. Kwon, H. Ham, K. B. Shim and H. W. Kim, *J. Mater. Chem.*, 2012, **22**, 17992.

42   K. Shen, X. Chen, J. Chen and Y. Li, *ACS Catal.*, 2016, **6**, 5887–5903.

43   M. Shen, C. Ruan, Y. Chen, C. Jiang, K. Ai and L. Lu, *ACS Appl. Mater. Interfaces*, 2015, **7**, 1207–1218.

44   G. Eda and M. Chhowalla, *Adv. Mater.*, 2010, **22**, 2392–415.

45   X. Xiang, X. Li, Z. Huang, T. Gao, H. Yuan and D. Xiao, *ChemElectroChem*, 2019, **6**, 1078–1087.

46   A. L. Patterson, *Phys. Rev.*, 1939, **56**, 978–982.

47   G. Fierro, M. Lo Jacono, M. Inversi, R. Dragone and P. Porta, *Top. Catal.*, 2000, **10**, 39–48.
48   Y. Yang, C. Wang, S. Gao, K. Mao, G. Xia, Z. Lin, P. Jiang, L. Hu and Q. Chen, *Nanoscale*, 2018, **10**, 21076–21086.
49   L. Zhang, Z. Su, F. Jiang, L. Yang, J. Qian, Y. Zhou, W. Li and M. Hong, *Nanoscale*, 2014, **6**, 6590–6602.
50   Y. Jiang, Y. Lu, X. Wang, Y. Bao, W. Chen and L. Niu, *Nanoscale*, 2014, **6**, 15066–15072.
51   H. Yu, A. Fisher, D. Cheng and D. Cao, *ACS Appl. Mater. Interfaces*, 2016, **8**, 21431–21439.
52   H. Bin Yang, J. Miao, S.-F. Hung, J. Chen, H. B. Tao, X. Wang, L. Zhang, R. Chen, J. Gao, H. M. Chen, L. Dai and B. Liu, *Sci. Adv.*, 2016, **2**, e1501122.
53   Z. Wang, H. Jin, T. Meng, K. Liao, W. Meng, J. Yang, D. He, Y. Xiong and S. Mu, *Adv. Funct. Mater.*, 2018, **28**, 1802596.
54   J. Wei, Y. Hu, Y. Liang, B. Kong, J. Zhang, J. Song, Q. Bao, G. P. Simon, S. P. Jiang and H. Wang, *Adv. Funct. Mater.*, 2015, **25**, 5768–5777.
55   Y. Jia, L. Zhang, A. Du, G. Gao, J. Chen, X. Yan, C. L. Brown and X. Yao, *Adv. Mater.*, 2016, **28**, 9532–9538.
56   H. Jiang, J. Gu, X. Zheng, M. Liu, X. Qiu, L. Wang, W. Li, Z. Chen, X. Ji and J. Li, *Energy Environ. Sci.*, 2019, **12**, 322–333.
57   Z. Zhu, Y. Yang, Y. Guan, J. Xue and L. Cui, *J. Mater. Chem. A*, 2016, **4**, 15536–15545.
58   M. De Koninck, S. Poirier and B. Marsan, *J. Electrochem. Soc.*, 2006, **153**, A2103.
59   A. Serov, N. I. Andersen, A. J. Roy, I. Matanovic, K. Artyushkova and P. Atanassov, *J. Electrochem. Soc.*, 2015, **162**, F449–F454.
60   D. Wang, C. Ao, X. Liu, S. Fang, Y. Lin, W. Liu, W. Zhang, X. Zheng, L. Zhang and T. Yao, *ACS Appl. Energy Mater.*, 2019, **2**, 6497–6504.
61   M. C. Biesinger, *Surf. Interface Anal.*, 2017, **49**, 1325–1334.
62   T. Sun, L. Xu, D. Wang and Y. Li, *Nano Res.*, 2019, **12**, 2067–2080.
63   S. Jung, C. C. L. McCrory, I. M. Ferrer, J. C. Peters and T. F. Jaramillo, *J. Mater. Chem. A*, 2016, **4**, 3068–3076.
64   Y. Zhang, L. Gao, E. J. M. Hensen and J. P. Hofmann, *ACS Energy Lett.*, 2018, **3**, 1360–1365.
65   Y. Zhu, H. C. H. M. Chen, C. S. Hsu, T. S. Lin, C. J. Chang, S. C. Chang, L. D. Tsai and H. C. H. M. Chen, *ACS Energy Lett.*, 2019, **4**, 987–994.
66   B. Seo, Y. J. Sa, J. Woo, K. Kwon, J. Park, T. J. Shin, H. Y. Jeong and S. H. Joo, *ACS Catal.*, 2016, **6**, 4347–4355.
67   D. S. Dhawale, S. Kim, D. H. Park, J. H. Choy, S. S. Al-deyab, K. Ariga, E. Kim and A. Vinu, *ChemElectroChem*, 2015, **2**, 497–502.